

# Optics Letters

## All-optical diffractive neural networked terahertz hologram

DASHUANG LIAO,<sup>1</sup> KA FAI CHAN,<sup>2</sup> CHI HOU CHAN,<sup>2,3</sup> QINGLE ZHANG,<sup>2,3</sup>  AND HAOGANG WANG<sup>1,\*</sup>

<sup>1</sup>College of Information Science and Electronic Engineering, Zhejiang University, Hangzhou 310027, China

<sup>2</sup>State Key Laboratory of Terahertz and Millimeter Waves, City University of Hong Kong, 999077, Hong Kong SAR, China

<sup>3</sup>Department of Electronic Engineering, City University of Hong Kong, 999077, Hong Kong SAR, China

\*Corresponding author: hgwang@zju.edu.cn

Received 31 March 2020; revised 18 April 2020; accepted 20 April 2020; posted 20 April 2020 (Doc. ID 394046); published 15 May 2020

Holography has garnered an explosion of interest in tremendous applications, owing to its capability of storing amplitude and phase of light and reconstructing the full-wave information of targets. Spatial light modulators, metalenses, metasurfaces, and other devices have been explored to achieve holographic images. However, the required phase distributions for conventional holograms are generally calculated using the Gerchberg–Saxton algorithm, and the iteration is time-consuming without Fourier transform or other acceleration techniques. Few studies on designing holograms using artificial intelligence methods have been conducted. In this Letter, a three-dimensional (3D)-printed hologram for terahertz (THz) imaging based on a diffractive neural network (DNN) is proposed. Target imaging letters “THZ” with uniform field amplitude are assigned to a predefined imaging surface. Quantified phase profiles are primarily obtained by training the DNN with the target image and input field pattern. The entire training process takes only 60 s. Consequently, the hologram, that is, a two-dimensional array of dielectric posts with variational heights that store phase information, is fabricated using a 3D printer. The full-wave simulation and experimental results demonstrate the capability of the proposed hologram to achieve high-quality imaging in the THz regime. The proposed lens and design strategy may open new possibilities in display, optical-data storage, and optical encryption. © 2020 Optical Society of America

<https://doi.org/10.1364/OL.394046>

Holograms that can arbitrarily generate complex wavefronts through inference of artificial meta-atoms are vital tools in physical acoustics [1], optical imaging [2–5], and information processing [6,7]. The conventional design methodology for holograms in terahertz (THz) is analogous to that in acoustic and optical regions. To generate anticipant pictures, light-matter interactions are typically realized through flexibly designed and distributed constituent subwavelength pixels. Dielectric lenses and metasurfaces are two popular and effective schemes. However, metasurface-based transmit arrays with a single metallic layer operate at THz optical spectra are difficult

to obtain  $2\pi$  phase coverage, and a transmission coefficient amplitude is restricted [8–10]. This limitation can be alleviated by cascading three or more layers. Unfortunately, the manufacture of stacked multilayer structures with the required precision in THz and optical ranges is challenging and high in cost [11,12]. As for dielectric lenses, modulations of the electromagnetic waves are implemented through phase accumulation over tunable propagation distance inside the materials, thereby resulting in a large thickness of the holograms. Nevertheless, such lenses can be fabricated with a quick, cost-efficient, and high-resolution 3D printing technique.

Holography was invented in 1947 [13], in which, a 3D image is reconstructed by recording wave interference scattered by an object and a coherent beam. However, this process functions only when both actual objects and coherent waves are present. Subsequently, a method called computer-generated holography was proposed [14], in which phase distribution is calculated directly at the air-hologram interface. The required phase distributions are generally calculated using the Gerchberg–Saxton (GS) algorithm whose iteration process is time-consuming without Fourier transform or other acceleration techniques. In Ref. [15], the final convergence of the GS algorithm is reached after about 100 iterations, which takes about 4 h. Besides, there are some breakpoints in the images. Furthermore, mastering the design skills is difficult for non-professionals, as such methods are based on profound theories in optics, electromagnetics, and applied mathematics. Few studies on designing holograms using artificial intelligence methods have been conducted.

In recent decades, artificial neural networks (ANNs) [16,17] have been explored as a powerful data-driven methodology for generalizing complex functions or data, which have significantly improved state-of-art speech and image recognition, as well as language translation, and gradually penetrated the disciplines of materials science and optics [18–22]. In Ref. [18], an ANN is used to simulate light scattering by multilayer nanoparticles with a runtime faster than that in numerical simulations by an order of magnitude. Reference [19] studied the forward prediction of optical responses and the inverse design of chiral metamaterials using deep learning. Most recently, the concept of diffractive deep neural network is proposed by Lin *et al.* [23], which is seen as a physical optical machine learning framework

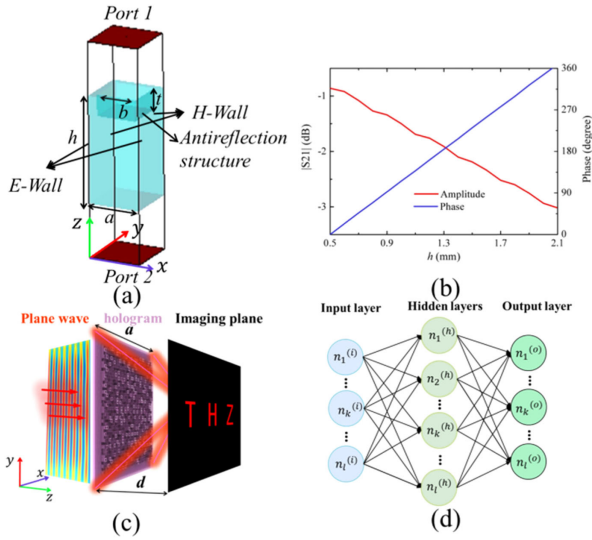


**Fig. 1.** (a) Illustration of the unit cell and simulation boundary conditions. (b) Simulated transmission amplitude and phase versus the element height. (c) Architecture of a THz hologram and work mechanism for imaging based on DNN. (d) Conventional neural network.

and employed to execute the inference tasks in MNIST and Fashion-MNIST datasets.

In this Letter, a 3D-printed hologram, designed by a DNN for THz imaging, is proposed and demonstrated. First, the target image and incident field patterns are fed into the DNN for training to obtain the required phase profiles. The entire training stage costs only 60 s using the TensorFlow framework and graphic processing unit acceleration. Secondly, the heights of the dielectric posts in the hologram are determined according to the trained transmission phases. Consequently, a 3D printer is used to print the hologram at a low cost. A hologram that can reconstruct a “THZ” image is fabricated. The simulated and measured electric field intensities agree very well and verify that the technique can generate images with uniform amplitude at high speed.

The unit cell of the hologram is depicted in Fig. 1(a), which is a square dielectric post with a lattice size of  $a = 0.5$  mm. The dielectric has a relative permittivity  $\epsilon_r = 2.66$  and a loss tangent  $\tan \delta = 0.03$ , which is measured using an EKSPILA THz time-domain spectroscopy at around 300 GHz [24]. Periodic unit cell simulation is performed with the commercial software CST. To reduce the reflection and weaken the effect of standing waves at the air-dielectric interface [25], a square hole, dug out on the top of the element, forms the quarter wavelength impedance transformer. Height  $t$  is calculated as follows:

$$t = \lambda_{\text{hole}}/4, \quad (1)$$

$$\lambda_{\text{hole}} = \lambda_0 / ((\epsilon_r)^{1/2})^{1/2}. \quad (2)$$

Therefore, height  $t = 0.196$  mm. The minimum reflection  $S_{11}$  is obtained by sweeping parameter width  $b$  in the simulation. The final optimized value  $b = 0.382$  mm. A normally incident  $x$ -polarized plane wave is used to excite the unit, and the transmitted  $x$ -polarized wave is recorded. As presented in Fig. 1(b), the amplitude of the transmission coefficient  $S_{21}$  is larger than  $-3$  dB, and the transmission phase is nearly a

linear function of the element height. With an increase in the height from 0.5 to 2.1 mm, the phase covers a range of approximately  $2\pi$ .

The schematic of the hologram and working principle are shown in Fig. 1(c). The hologram is regarded as a hidden layer in the conventional ANN, as shown in Fig. 1(d). Each discrete dielectric element inside the hologram corresponds to a neuron; the incident and output fields are regarded as input and output layers, respectively. According to the Huygens principle, each particle of a wavefront can be treated as the center of a secondary wave source. Thus, one layer connects the next layer by diffraction, a fully connected DNN with a large axial distance  $d = 20$  mm between the hologram and image plane is constructed. The optical mode of the  $i$ th element with a coordinate  $(x_i, y_i, z_i)$  on the hologram is given by the Rayleigh–Sommerfeld diffraction equation:

$$w_i(x, y, z) = \frac{d}{r^2} \left( \frac{1}{2\pi r} + \frac{1}{j\lambda} \right) \exp \left( \frac{j2\pi r}{\lambda} \right), \quad (3)$$

where  $\lambda$  is the wavelength of the incident wave in vacuum, and  $r = ((x - x_i)^2 + (y - y_i)^2 + (z - z_i)^2)^{1/2}$  denotes the propagation distance. The output  $n_i(x, y, z)$  of the element located at  $(x_i, y_i, z_i)$  is modeled as follows:

$$n_i(x, y, z) = w_i(x, y, z) \cdot t_i(x_i, y_i, z_i) \cdot m_i(x_i, y_i, z_i). \quad (4)$$

In Eq. (4),  $t_i(x_i, y_i, z_i)$  denotes the complex transmission coefficient, i.e.,  $t_i(x_i, y_i, z_i) = \alpha_i(x_i, y_i, z_i) \exp(j\phi_i(x_i, y_i, z_i))$ , which composes two parts, namely, amplitude  $\alpha_i(x_i, y_i, z_i)$  and phase  $\phi_i(x_i, y_i, z_i)$ , and  $m_i(x_i, y_i, z_i) = \sum_k n_k^{\text{last}}(x_i, y_i, z_i)$  is defined as the superposition of the output from all the elements in the last layer to element  $i$ . The intensity in the output plane is  $f_k^{\text{out}} = |m_k^{\text{out}}|^2$ . The loss function uses a mean squared error to measure the distance between the ratio of energy at imaging points  $f_k^{\text{out}}$  to the sum of energy on the output plane  $\sum_{\text{all}} f_k^{\text{out}}$ , and the ratio of the goal label intensity distribution  $g_k^{\text{label}}$  to the sum of goal label intensities on the imaging plane  $\sum_{\text{all}} g_k^{\text{label}}$ . The loss function can be written as follows:

$$L(\phi_i) = \frac{1}{K} \sum_k \left| \frac{f_k^{\text{out}}}{\sum_{\text{all}} f_k^{\text{out}}} - \frac{g_k^{\text{label}}}{\sum_{\text{all}} g_k^{\text{label}}} \right|^2, \quad (5)$$

where  $K$  refers to the total number of sampling points in the output plane. To image the letters, the goal label intensity is set to 1 in the bright region and 0 elsewhere. The problem is described as follows:

$$\min L(\phi_i), \quad \text{s.t. } 0 \leq \phi_i \leq 2\pi. \quad (6)$$

To demonstrate the feasibility of the technique, a proof-of-concept test case is designed to reconstruct the “THZ” holographic image, as shown in Fig. 2(a). The hologram is composed of  $60 \times 60$  cells, covering an area of  $30 \times 30$  mm<sup>2</sup>. Random initialized phase profiles  $\phi_i$  are updated using an error back propagation algorithm combined with the Adam adaptive moment estimation optimizer [26] with a learning rate of 0.01. The calculated field distributions after 10, 100, and 1000 epochs are presented in Figs. 2(b)–2(d). The 100-iteration step already produced reasonable intensity profiles, but side-lobes surround the target pattern along with small variations in amplitude over the pattern itself. Figure 2(e) shows that the

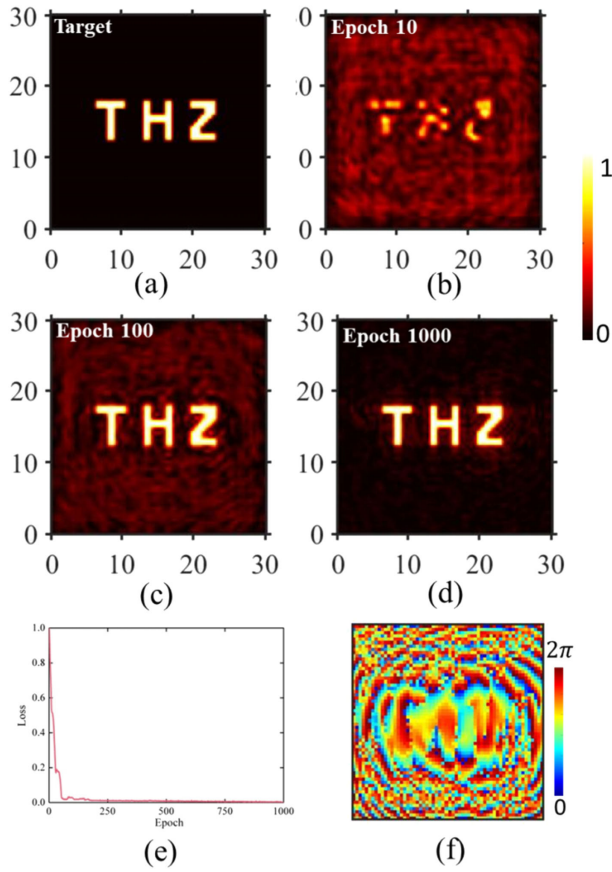


**Fig. 2.** (a) Target intensity profile. (b)–(d) Calculated holographic image over different training stages. (b) Epoch 10. (c) Epoch 100. (d) Epoch 1000. (e) Training loss versus epoch. (f) Optimized phase profile.

normalized loss value decreases gradually to a stable value after the final convergence in epoch 1000. The reconstructed image of 1000 iterations has uniform amplitudes with low-noises. The optimized phase profiles are shown in Fig. 2(f). Notably, the entire training stage takes only approximately 60 s using the TensorFlow (v1.3.0, Google Inc.) framework, Python (v3.5.0), and a graphical processing unit (TITAN X).

The model and normalized electric field intensities simulated through the commercial software, i.e., CST Microwave Studio 2018, are plotted in Fig. 3. Full-wave simulation is conducted with the time-domain solver in CST, and perfectly matched layer boundary conditions are set in the  $x$ ,  $y$ , and  $z$  directions. When an  $x$ -polarized plane wave incidents normally on the hologram, the dominating component is  $E_x$ , which is the co-polarization of the incident wave. Since the amplitudes of the  $E_y$  and  $E_z$  are too small to be ignored, the intensity of the electric field is treated as  $|E_t| = (|E_x|^2 + |E_y|^2 + |E_z|^2)^{1/2} \approx |E_x|$ . The tailored phase distributions of the holograms in Fig. 2(f) are modeled by using a linear map of the post height  $h_p$  and the transmission phase  $\varphi_t$ :  $h_p = \varphi_t/236.8$ , where 236.8 is just the average slope of the blue line in Fig. 1(b). Thus, it is easy to convert the phase profiles into height distributions. An additional uniform thickness of 0.5 mm is added to each element, and a frame with a width of 5 mm is employed to facilitate hologram fabrication and testing.

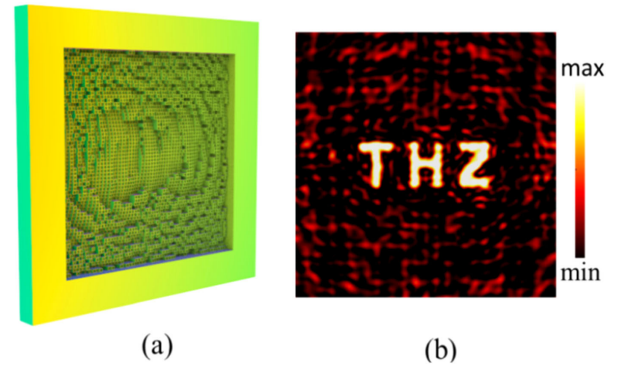


**Fig. 3.** (a) Model illustration in CST. (b) Simulated normalized electric field intensity on an imaging plane.

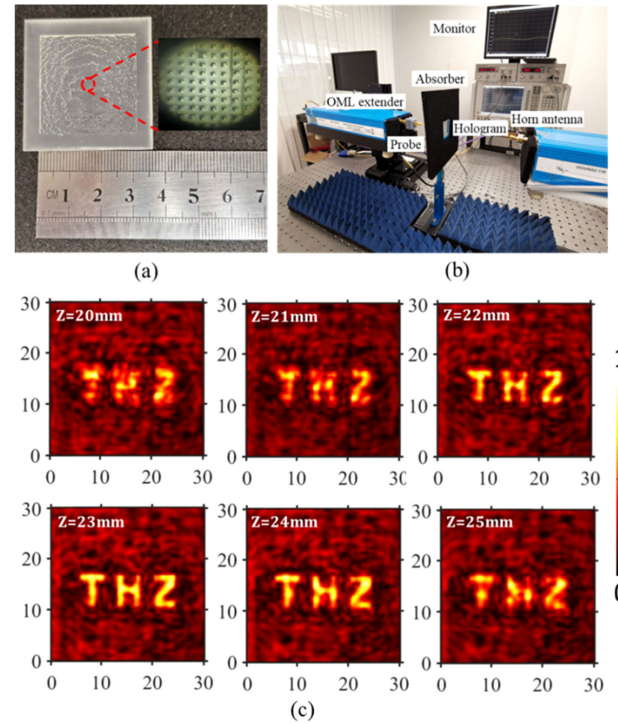


**Fig. 4.** (a) Photograph of a fabricated hologram with a magnified view under a microscope. (b) Experiment setup. (c) Measured intensity profiles at different positions at 300 GHz.

A 3D printing technique is utilized to simplify the fabrication process and reduce cost. The 3D printer, i.e., Form2 from Formlabs [27], has a fundamental resolution of 25  $\mu\text{m}$ , and the laser spot size is 140  $\mu\text{m}$ . A prototype of the proposed hologram is presented in Fig. 4(a) with a magnified view of the details under a microscope, and it takes 204 min to finish the fabrication. As illustrated in Fig. 4(b), a near-field scanning experiment setup is built to measure the transverse intensity patterns. The horn antenna is utilized to generate the plane wave, and a small open-ended waveguide probe scans the imaging plane at a pre-defined position to receive energy with a scanning resolution of 0.5 mm in the transverse plane.

As mentioned above, the  $|E_y|$  and  $|E_z|$  components are neglected; hence, only  $|E_x|$ , the co-polarization component, is measured. As shown in Fig. 4(c), the intensity profiles of the



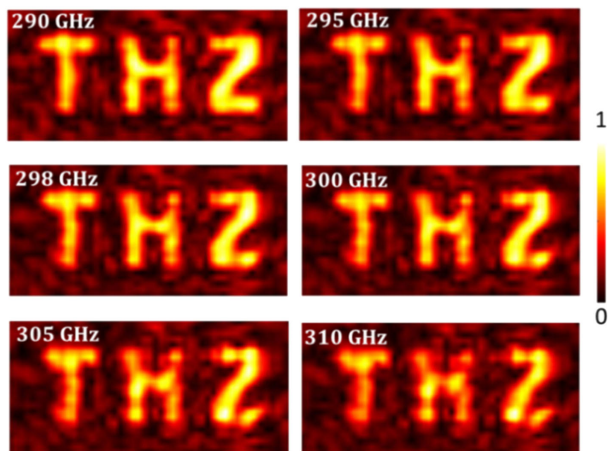


**Fig. 5.** Measured imaging performance at  $z = 23$  mm for different frequencies.

positions from 20 to 25 mm are measured at 300 GHz, and the “THZ” holographic images can be experimentally observed. The image closest to the simulated result locates at  $z = 23$  mm with diffraction efficiency 30.56%, slightly deviating from the preset distance  $z = 20$  mm. Discrepancies are caused by the uncertainties in dielectric property, fabrication imperfections, and phase profile deviations from that of an ideal plane wave. Note that in the experiment we use a spherical beam with a large radius to approximate the plane wave. Furthermore, the broadband property is also investigated. The magnitudes of the electric fields at  $z = 23$  mm from 290 to 310 GHz are illustrated in Fig. 5. Similar imaging effects are observed. This phenomenon relies essentially on the linear phase response of the unit. Phase accumulation does not deviate considerably, as the frequency varies in the frequency range.

In conclusion, a physical level all-optical DNN for hologram imaging in THz is proposed and fabricated for the first time, to the best of our knowledge. The required phase profiles of the DNN hologram lens are trained using the artificial intelligence methods. The simulated and experimental results at 300 GHz demonstrate that the proposed lens can produce the desired intensity pattern on a predefined image plane. The designed hologram may find applications in wireless communication and optical-data storage. Moreover, the design method can be readily scaled up to optical ranges or down to microwave ranges.

**Funding.** National Natural Science Foundation of China (61231001, 61471316); National Basic Research Program of China (973 Program) (2014CB340005); Hong Kong Research Grants Council Theme-based Research Scheme (T42-103/16-N).

**Disclosures.** The authors declare no conflicts of interest.

## REFERENCES

1. M. Brown, *Appl. Phys. Lett.* **115**, 053701 (2019).
2. J. Han, L. Li, S. Tian, G. Liu, H. Liu, and Y. Shi, *IEEE J. Emerg. Sel. Top. Circuits Syst.* **10**, 52 (2020).
3. L. Huang, X. Chen, H. Mühlenbernd, H. Zhang, S. Chen, B. Bai, Q. Tan, G. Jin, K.-W. Cheah, C.-W. Qiu, J. Li, T. Zentgraf, and S. Zhang, *Nat. Commun.* **4**, 2808 (2013).
4. W. Zhao, B. Liu, H. Jiang, J. Song, Y. Pei, and Y. Jiang, *Opt. Lett.* **41**, 147 (2016).
5. L. Li, T. Cui, W. Ji, S. Liu, J. Ding, X. Wan, Y. Li, M. Jiang, C.-W. Qiu, and S. Zhang, *Nat. Commun.* **8**, 1 (2017).
6. J. Li, S. Kamin, G. Zheng, F. Neubrech, S. Zhang, and N. Liu, *Sci. Adv.* **4**, eaar6768 (2018).
7. Y. Xing, M. Kaaniche, B. Pesquet, and F. Dufaux, *Digital Holographic Data Representation and Compression* (Academic, 2015).
8. L. Liu, X. Zhang, M. Kenney, X. Su, N. Xu, C. Ouyang, Y. Shi, J. Han, W. Zhang, and S. Zhang, *Adv. Mater.* **26**, 5031 (2014).
9. X. Zhang, Z. Tian, W. Yue, J. Gu, S. Zhang, J. Han, and W. Zhang, *Adv. Mater.* **25**, 4566 (2013).
10. F. Monticone, N. Mohammadi Estakhri, and A. Alù, *Phys. Rev. Lett.* **110**, 203903 (2013).
11. T. Cai, G.-M. Wang, X.-L. Fu, J.-G. Liang, and Y. Zhuang, *IEEE Trans. Antennas Propag.* **66**, 3219 (2018).
12. S. Liu, A. Noor, L. Du, L. Zhang, Q. Xu, K. Luan, T. Wang, Z. Tian, W. Tang, J. Han, W. Zhang, X. Zhou, Q. Cheng, and T. Cui, *ACS Photonics* **3**, 1968 (2016).
13. D. Gabor, *Nature* **161**, 777 (1948).
14. C. Slinger, C. Cameron, and M. Stanley, *Computer* **38**, 46 (2005).
15. J. Gospodarcic, A. Kuzmenko, A. Pimenov, C. Huber, D. Suess, S. Rotter, and A. Pimenov, *Appl. Phys. Lett.* **112**, 221104 (2018).
16. Y. LeCun, Y. Bengio, and G. Hinton, *Nature* **521**, 436 (2015).
17. J. Schmidhuber, *Neural Networks* **61**, 85 (2015).
18. J. Peurifoy, Y. Shen, L. Jing, Y. Yang, F. Cano-Renteria, B. G. DeLacy, J. D. Joannopoulos, M. Tegmark, and M. Soljačić, *Sci. Adv.* **4**, eaar4206 (2018).
19. W. Ma, F. Cheng, and Y. Liu, *ACS Nano* **12**, 6326 (2018).
20. R. González Ayestarán, *IEEE Antennas Wireless Propag. Lett.* **17**, 1233 (2018).
21. G. Carleo and M. Troyer, *Science* **355**, 602 (2017).
22. C. Gianfagna, H. Yu, M. Swaminathan, P. Raj, R. Tummala, and G. Antonini, *J. Electron. Mater.* **46**, 1 (2017).
23. X. Lin, Y. Rivenson, N. T. Yardimci, M. Veli, Y. Luo, M. Jarrahi, and A. Ozcan, *Science* **361**, 1004 (2018).
24. K. B. Ng and C. H. Chan, *Terahertz Sci. Technol. Int. J. THz* **9**, 45 (2016).
25. H. Yi, S. Qu, K. Ng, C. H. Chan, and X. Bai, *IEEE Trans. Antennas Propag.* **64**, 442 (2016).
26. D. P. Kingma and J. Ba, “Adam: A Method for Stochastic Optimization,” arXiv:1412.6980 (2014).
27. Formlabs <https://formlabs.com/>.